Check for updates

Nanocube In₂O₃@RGO heterostructure based gas sensor for acetone and formaldehyde detection†

Rajneesh Kumar Mishra, [iD] ‡[a] G. Murali,[a] Tae-Hyung Kim,[b] Jee Hun Kim,[b] Young Jin Lim,[a] Byoung-Suhk Kim,[c] P. P. Sahay[d] and Seung Hee Lee*[a]

Here, we studied the gas sensing response properties for acetone and formaldehyde by a chemiresistive nanocube In₂O₃@RGO heterostructure sensor. The nanocube In₂O₃@RGO heterostructure based sensor demonstrates a high response to acetone (∼85%) and formaldehyde (∼88%) at 25 ppm concentration and optimum working temperatures of 175 °C and 225 °C, respectively. Additionally, we examined the influence of potential barrier heights in the response/recovery time of the nanocube In₂O₃@RGO heterostructure based acetone and formaldehyde gas sensor. The real-time response/recovery analysis reveal that the sensor response depends on the potential barrier height as well as adsorbed active sites (O_2^- & O^-) on the sensor surface. Furthermore, the nanocube In₂O₃@RGO heterostructure based gas sensor shows good selectivity to acetone and formaldehyde at optimum working temperature of 175 °C and 225 °C, respectively, compared to the other interfering gases such as ethanol, methanol, chloroform, toluene, benzene, ammonia, formic acid and acetic acid. The life-time analysis has been performed for 30 days, which showes the stability of nanocube In₂O₃@RGO heterostructure based acetone and formaldehyde sensor.

Introduction

The increasing anxiety about the consequences of air pollution with respect to public health has led to a high demand for solid state gas sensors in domestic, military and industrial applications.[1] Major interest has arisen in the field of selective gas detection of volatile organic compounds (VOCs) from the environment in the presence of various interfering gases.[2–4] Chemical industries use VOCs for a variety of purposes, which enters into the human body through breathing and passes *via* the bloodstream into many organs, adversely affecting the brain, nervous and skin systems, even at very low concentrations.[4,5]

Acetone [(CH₃)₂CO], a widely used VOC in laboratories as well as in industries, is toxic to human organs and is a selective breath marker for type-1 diabetics.[6] The healthy breath environment contains less than 0.9 ppm concentration of acetone. But it indicates high level of ketone in the blood (ketosis) in insulin-dependent diabetes if its concentration exceeds 1.8 ppm in living places.[7] On the other hand, formaldehyde (HCHO), the most abandoned airborne carbonyl chemical which is extensively used in the decoration of wood furnitures in daily-life and industrial manufacturing processes, is recognized as one of the most serious pollutants in the indoor environment and causes headache, coryza, sick house syndromes, nausea, childhood asthma and even lung cancer.[8,9] Therefore, for the safety point of view fast, accurate and rapid monitoring of these health hazardous and environmental pollutant gases from the public places with an effective and convenient method are of significant practical importance.

Among metal oxide semiconductors (MOS), indium oxide (In₂O₃) is a wide direct band gap ($E_g = 3.7$ eV)[9] and indirect band gap ($E_g = 2.5$ eV)[10] semiconductor, having outstanding optical and electrical properties. It is a robust candidate from the transparent semiconducting oxide family and one of the most promising and applicable material. In₂O₃ is immersed as a next generation solid state gas sensor due to its good performance and ease of use. It is extensively used in various fields such as solar cell,[11] supercapacitor,[12] field effects transistors,[13] transparent thin film transistors,[14] photo-catalyst,[15] flat panel display,[16] light-emitting diodes,[17] and biological and chemical gas sensors.[18,19] In₂O₃ nanostructure offers a hopeful platform for high performance gas sensing devices that employ direct

[a]*Applied Materials Institute for BIN Convergence, Department of BIN Fusion Technology, Department of Polymer-Nano Science and Technology, Chonbuk National University, Jeonju, Jeonbuk 561-756, Korea. E-mail: lsh1@chonbuk.ac.kr; Tel: +82-63-270-2343*

[b]*Graduate School of Flexible & Printable Electronics Engineering, Chonbuk National University, Jeonju, Jeonbuk 561-756, Korea*

[c]*Department of Organic Materials & Fiber Engineering, Department of BIN Fusion Technology, Chonbuk National University, Jeonju, Jeonbuk 561-756, Korea*

[d]*Department of Physics, Motilal Nehru National Institute of Technology Allahabad, Allahabad-211004, India*

† Electronic supplementary information (ESI) available. See DOI: 10.1039/c7ra05685k

‡ Current Affiliation: Department of Electronics Engineering, Incheon National University, Incheon, 406–772, Korea.

electrical readout and used to detect the harmful, toxic and explosive gases.[20–22]

Graphene is an attractive material both as the benchmark of fundamental physical properties of a two-dimensional system and its widespread applications in the field of material science & nanotechnology.[23,24] Currently, it is one the most important material and being targeted for a number of commercial & industrial applications. It is also successfully demonstrated in flexible chemoresistive sensor,[25] organic light emitting diodes,[26] liquid crystal displays,[27] organic photovoltaic,[28] energy storage[29] and touch screens,[30] etc. Recently, noteworthy progress has been achieved that attracted much attention towards the development of different kinds of gas sensors using graphene, reduced graphene oxide (RGO), and graphene/MOS hybrid nanostructures. Some et al. have reported highly sensitive and selective gas sensor using the hydrophilic and hydrophobic graphene.[31] Sun et al. have investigated the nanocasting synthesis of In_2O_3 with appropriate mesostructured ordering and enhanced gas-sensing property.[32] Ju et al. have studied the single-carbon discrimination by preferred peptides for the individual detection of VOCs.[33] Moon et al. have presented the highly transparent, self-assembled nanocolumnar tungsten oxide thin films based sensor for NO_2 and VOCs with detection limits below parts per trillion.[34] Lai et al. have demonstrated the improved formaldehyde gas sensing performance based on ordered arrays of bead-chain-like In_2O_3 nanorods.[35] Yang et al. synthesized the additive free In_2O_3 cubes embedded with graphene and studied improved NO_2 sensing performance at room temperature.[36] Huang et al. have synthesized ZnO QDs/ graphene nanocomposites and studied the room temperature formaldehyde sensing properties with improved performance and fast response and recovery times.[37] Recently our group, Mishra et al. have studied the highly sensitive, selective and stable H_2 & LPG gas sensor based on RGO/SnO_2 QD hybrid nanostructure.[38]

The RGO/MOS hybrid nanostructures have been explored for the application in solid state chemical gas sensors with high response and reliability. Nevertheless, the sensing properties of RGO/MOS hybrid nanostructures, such as the high test gas response, good selectivity & stability as well as quick response/ recovery time are the vital parameters for actual gas sensor operation, which require further improvements. In the present study, we have successfully demonstrated the optimum working temperature and concentration for which nanocube $In_2O_3@$ RGO heterostructure based gas sensor exhibits maximum response to acetone and formaldehyde. We have also displayed the selectivity and stability of nanocube $In_2O_3@RGO$ heterostructure based gas sensor at that particular gas response temperature and concentration. The gas sensor mechanisms of adsorption–desorption and theoretical calculation of the active sites O_2^- and O^-, which are participating in the sensing mechanism at various operating temperature have been studied. Although, we have performed the number of experiments at which nanocube $In_2O_3@RGO$ heterostructure based gas sensor describes good gas sensing properties to achieve the optimum working temperature (175 °C & 225 °C) for 25 ppm concentration.

Experimental details

Materials and synthesis

Reduced graphene oxide (RGO) was synthesized from graphite powder purchased from the Alfa Aesar using the modified Hummers method.[23,24] The In_2O_3 and nanocube $In_2O_3@RGO$ heterostructure were prepared by one step hydrothermal process. In this method firstly, (20 mmol) of $InCl_3$ was dissolved in distilled water to form a colorless transparent solution and then 1.5 mg RGO was added to the above solution. Consequently, with mild stirring, 1 ml hexamethyldisilazane (HMDS) surfactant was added to the above solution at room temperature. Further, the pH was maintained at 9 by adding the NaOH solution drop wise into the above solution. The entire solution was transferred into a 100 ml Teflon-lined stainless steel autoclave to react at 120 °C for 20 h and then allowed to naturally cooled up to room temperature. The obtained precipitate was separated by centrifuging at 4000 rpm for 30 minutes and washed with distilled water and ethanol several times to remove impurity ions and then dried at 70 °C for 4 hours in a hot air oven. Finally, the obtained precipitate was annealed at 400 °C for 1 hour to obtain the desire products nanocube $In_2O_3@RGO$ heterostructure. The dried mass was then crushed into the fine powder for further characterizations. Following the above-mentioned process bare In_2O_3 was also synthesized. The fine powder of nanocube $In_2O_3@RGO$ heterostructure, RGO and In_2O_3 were pressed into pellet of 10.5 mm diameter and 1.0 mm thickness at a pressure of ~15 MPa using a hydraulic press. These pellets were further sintered at 200 °C for 30 minute. After that, a high-temperature silver paste was used for making the Ohmic contact on both surfaces of pellet.

Materials characterization

The phase identification of the nanocube $In_2O_3@RGO$ heterostructure was carried out by powder X-ray diffraction (XRD) using Bruker AXS C-8 advanced diffractometer with Cu K_α radiation ($\lambda = 1.5406$ Å). The X-ray photoelectron spectroscopy (XPS) analysis has been done by a K_α Thermo Scientific equipped with a monochromatic Al-Ka X-ray and 100–4000 eV ion gun. The Raman spectrum was recorded by Lab RAM HR 800 microlaser Raman system in backscattering geometry using the 514.5 nm line of Ar^+-laser as an excitation source. The morphological and elemental composition was probed by JEOL field electron scanning electron microscope (FE-SEM) along with elemental mapping. The shape and structure were investigated by transmission electron microscope (TEM) on a Philips model Tecnai-20 using an accelerating voltage of 200 kV. The experimental characterization techniques were also performed for bare RGO and In_2O_3 nanocube samples and corresponding results are presented in ESI.†

Gas sensing measurements

The acetone and formaldehyde gas sensing properties of nanocube $In_2O_3@RGO$ heterostructure based gas sensor have been determined by measuring the change in electrical

resistance of sensing device and estimated by the following equation:[38]

$$S = \frac{R_{\text{air}} - R_{\text{acetone/formaldehyde}}}{R_{\text{air}}} \times 100\% \tag{1}$$

where $R_{\text{acetone/formaldehyde}}$ and R_{air} are the resistances under acetone & formaldehyde and air.

To measure quantitatively the concentration (ppm) of acetone and formaldehyde, the following method has been used. If V is the volume of the test gas chamber and C_{ppm} is the concentration of acetone and formaldehyde, then the volume of acetone and formaldehyde in the test gas chamber is,[5]

$$V_{\text{acetone/formaldehyde}} = C_{\text{ppm}} \times V \tag{1a}$$

So, the number of moles of acetone and formaldehyde, respectively into the test gas chamber can be defined as,

$$n_{\text{acetone/formaldehyde}} = \frac{PV_{\text{acetone/formaldehyde}}}{RT} = \frac{PC_{\text{ppm}}V}{RT} \tag{1b}$$

$M_{\text{acetone/formaldehyde}}$ and $\rho_{\text{acetone/formaldehyde}}$ are the molar mass and density of acetone & formaldehyde. Then, the final volume of liquid acetone and formaldehyde ($V_{\text{a,f}}$), respectively are injected into the test gas chamber is given as:

$$V_{\text{a,f}} = \frac{M_{\text{acetone/formaldehyde}} n_{\text{acetone/formaldehyde}}}{\rho_{\text{acetone/formaldehyde}}}$$

$$= \frac{M_{\text{acetone/formaldehyde}} PC_{\text{ppm}}V}{\rho_{\text{acetone/formaldehyde}} RT} \tag{1c}$$

By incorporating the values of $M_{\text{acetone/formaldehyde}}$, P, C_{ppm}, V, $\rho_{\text{acetone/formaldehyde}}$ and R in the eqn (1c) for both acetone and formaldehyde, respectively we get two separate equations:

$$V_{\text{acetone}} = 2.13 \left(\frac{C_{\text{ppm}}}{T} \right) \, \mu\text{L} \, \text{K} \tag{1d}$$

$$V_{\text{formaldehyde}} = 1.07 \left(\frac{C_{\text{ppm}}}{T} \right) \, \mu\text{L} \, \text{K} \tag{1e}$$

Therefore, the desired volumes of liquid acetone and formaldehyde at different operating temperature and concentration were calculated by using eqn (1d) and (1e) and injected into the test gas chamber by Hamilton micro-syringe.

Results and discussion

Structural studies

The phase/crystalline nature of the nanocube In₂O₃@RGO heterostructure was investigated by XRD pattern. Fig. 1(a) represents the XRD spectrum obtained from In₂O₃@RGO heterostructure annealed at 400 °C. All the diffraction peaks are indexed to the cubic structure of In₂O₃ and well matched with JCPDS card no. 71-2194 along with a peak corresponding to RGO observed at 23.48° (a broad shoulder, lattice spacing of 0.37 nm). The XRD spectra of RGO and In₂O₃ nanocubes were
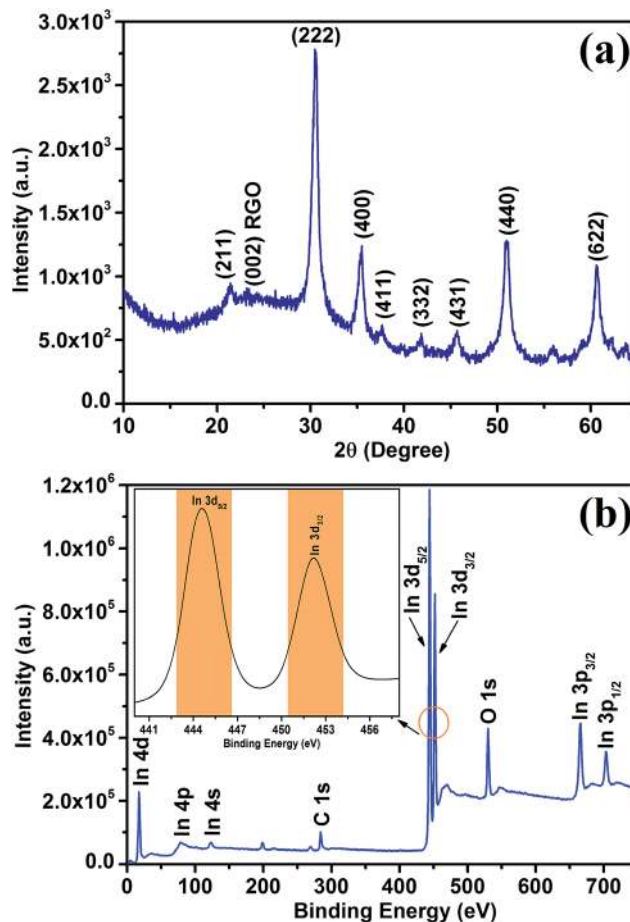

Fig. 1 Typical XRD pattern (a) and XPS spectrum (b) of as obtained nanocube In₂O₃@RGO heterostructure (inset in (b) depicts the convoluted characteristic peaks of In 3d).

also studied to confirm the structure and reported in ESI [Fig. S1†].

In order to confirm the elemental composition, the nanocube In₂O₃@RGO heterostructure was characterized by X-ray photoelectron spectroscopy (XPS). Fig. 1(b) shows the XPS survey spectrum of In₂O₃@RGO heterostructure. The In₂O₃@RGO heterostructure shows the presence of In (3p, 3d, 4s, 4p, 4d), O (1s) and carbon C (1s) peaks. The inset in Fig. 1(b) displays the high resolution spectrum of In 3d peak, which is ascribed to the characteristic spin–orbit split In $3d_{5/2}$ (444.24 eV) and In $3d_{1/2}$ (452.03 eV) and thus signified the presence of In₂O₃ in In₂O₃@RGO heterostructure.[39] The peak around 529.94 eV could be indexed to oxygen anions from In₂O₃.[40] Therefore, these results give the insight that the heterostructure was composed of RGO and In₂O₃ nanocube. XPS result confirms the successful formation of In₂O₃@RGO heterostructure and validates XRD findings. The XPS survey spectra of RGO and In₂O₃ nanocube were addressed in the ESI [Fig. S2†].

To further study the crystalline nature and defect states in In₂O₃@RGO heterostructure, Raman measurement was performed. Fig. 2 shows the Raman spectrum of as prepared nanocube In₂O₃@RGO heterostructure. The bands at 304 cm⁻¹ (E_{1g}), 362 cm⁻¹ (E_{2g}), 493 cm⁻¹ (A_{1g}) and 624 cm⁻¹ (E_{2g}) are
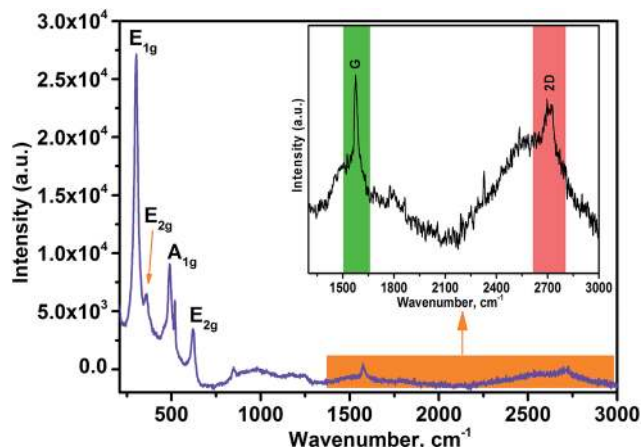
Fig. 2 Raman spectrum of nanocube In_2O_3@RGO heterostructure (inset shows the convoluted spectrum of RGO).

Raman active phonon modes of In_2O_3 nanocube. Furthermore, inset in Fig. 2 gestures the existence of carbon peaks in In_2O_3@RGO heterostructure, having G (1579 cm^{-1}) and 2D (2713 cm^{-1}) phonon modes. The G (1579 cm^{-1}) and 2D Raman phonon modes are related to the in-plane optical vibration of sp^2-bonded carbon atoms (degenerate zone center, E_{2g} mode) and second-order zone boundary phonons (representing defect states), respectively.[41] The Raman study outlines the validation of XRD and XPS result of In_2O_3@RGO heterostructure. Raman spectra of RGO and In_2O_3 nanocube are also interpreted and shown in ESI [Fig. S3†] to further confirm the XRD results of Fig. S1.†

The morphological and structural studies of nanocube In_2O_3@RGO heterostructure were evaluated by TEM, HRTEM and SAED pattern Fig. 3(a–d). TEM images in Fig. 3(a and b) indeed represent the small dark In_2O_3 nanocube decorated on the surface of RGO and inhibited re-stacking of RGO into multi-layers. Fig. 3(a and b) allude the good distribution of In_2O_3 nanocube on the RGO surface and manifested that RGO can be used as the substrate to synthesize In_2O_3@RGO heterostructure. The HRTEM image [Fig. 3(c)] shows the lattice plane of RGO (002) with spacing (0.37 nm) garlanded by two different planes (222) and (400) of In_2O_3 nanocube with spacing 0.29 nm and 0.25 nm, respectively, which again justified the XPD, XPS and Raman results. Fig. 3(d) displays the SAED pattern of nanocube In_2O_3/RGO heterostructure, suggesting poly-crystalline nature with different lattice planes of RGO and In_2O_3 nanocube. The lattice planes corresponding to (400), (431) and (622) indicated by diffused ring in Fig. 3(d) are recognized as In_2O_3 cubic phase whereas lattice plane (002) corresponds to RGO with lattice spacing 0.37 nm. These results also support the XRD analyses and are in good agreement with XPS and Raman results. Therefore, we can easily say that In_2O_3 nano-cubes (cubic structure) veneered on the RGO surface are poly-crystalline in nature. It is also noticed that each In_2O_3 nanocube attached to several other nanocubes as shown in Fig. 3(a and b). Thus, the good contact between the In_2O_3 nanocubes and RGO could efficiently minimize the electrical segregation of hetero-structure during the gas sensing measurements. The RGO with high surface area loaded with In_2O_3 nanocube can boost elec-tron transfer during the chemisorption process of the gas sensing mechanisms. All these above results confirm the successful formation of In_2O_3@RGO heterostructure. Further, the nanostructure of RGO and In_2O_3 nanocubes were also studied by TEM, HRTEM and SAED and represented in ESI [Fig. S4†]. The FE-SEM and corresponding elemental mapping of nanocube In_2O_3@RGO heterostructure, RGO and bare In_2O_3 nanocubes have been investigated for the morphological and elemental compositional analysis and depicted in ESI [Fig. S5†].

Gas sensing properties

Acetone and formaldehyde sensing study. The acetone and formaldehyde gas sensing properties of nanocube In_2O_3@RGO heterostructure based gas sensor have been investigated at different operating temperature (125–225 °C) with various concentration (5–25 ppm). The response of graphene, semi-conductor and graphene/semiconductor hybrid materials are deeply affected by operating temperature and the test gas concentration. Therefore, the kinetics of atmospheric oxygen adsorption and its reaction with test gas molecules on the surface of nanocube In_2O_3@RGO heterostructure based gas sensor has been studied by fluctuations in heterostructure materials resistance. To observe the optimum working temperature and test gas concentration under the relative humidity of ~53%, the response of the gas sensor fabricated by nanocube In_2O_3@RGO heterostructure has been examined as a function of operating temperature (125–225 °C) for different test gas concentration (5–25 ppm) as shown in Fig. 4(a and b). In Fig. 4(a and b), the dotted points are experimental data and solid lines are corresponding linear fittings.

In Fig. 4(a), the acetone response increases very quickly at 175 °C and achieves its maximum value (~85%) for 25 ppm. It
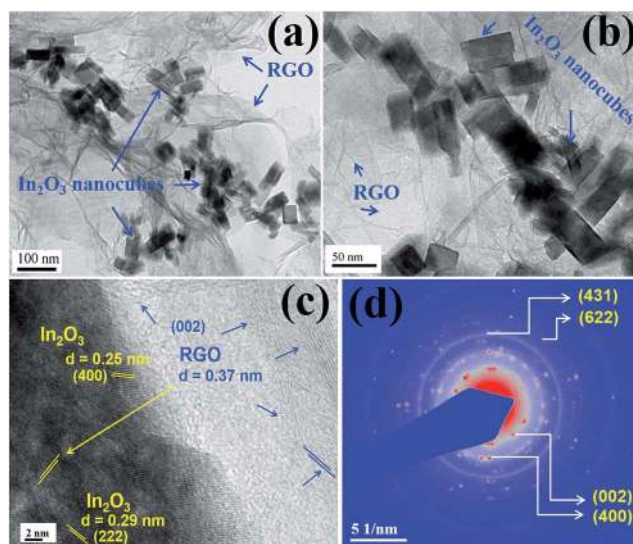

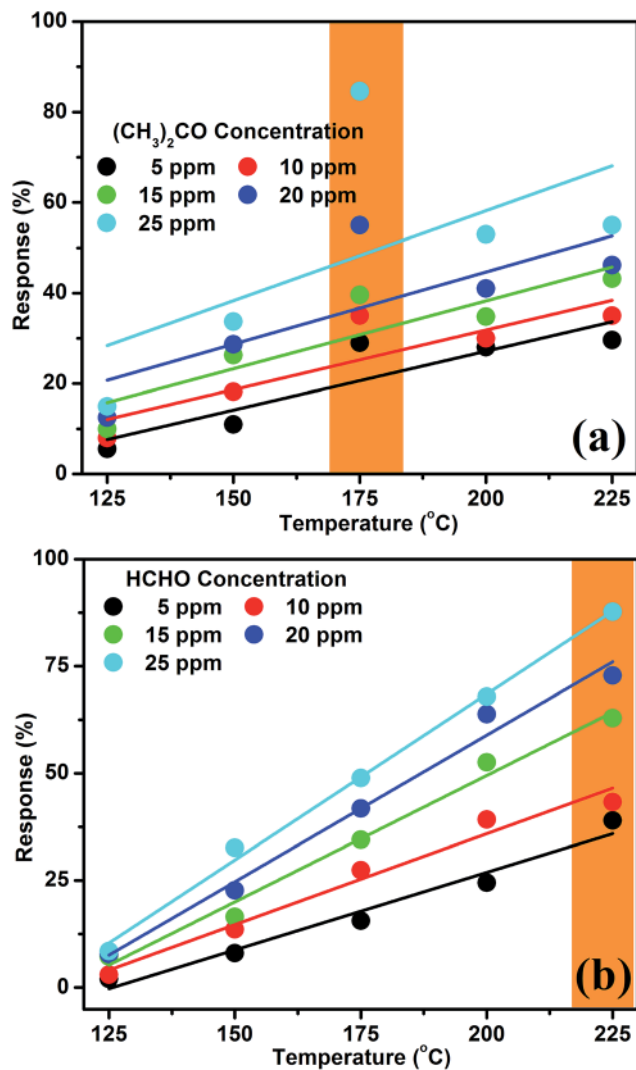**Fig. 3** TEM images (a and b), HRTEM image (c) and SAED pattern (d) of nanocube In_2O_3@RGO heterostructure.

Fig. 4 Response characteristics of acetone (a) and formaldehyde (b) based on the nanocube In_2O_3@RGO heterostructure sensor as a function of operating temperature for distinct test gas concentrations.

may be due to the presence of mixed state of active sites O_2^- and O^- at moderate operating temperature or good interaction of sensor surface with the test gas molecules. In other words, we can say that the reactivity of nanocube In_2O_3@RGO heterostructure based gas sensor surface with acetone needs definite activation energy which is provided by the tuning of working temperature. Hence, different kinds of gases are required different activation energies to work out for high performance gas sensor.[42] Therefore, we can infer that the highest response (~85%) at 175 °C for 25 ppm concentration is due to the insertion of RGO and hence it improves the surface reactivity of nanocube In_2O_3@RGO heterostructure based gas sensor. Consequently, it also enables the important role of active sites (O_2^- and O^-) [Table 1] and potential barrier heights [Table 2] in the sensing mechanisms. On the other hand, at low operating temperature (<175 °C), the sensor response of acetone is found to be low (<40%), which may be due to the strong potential

barrier formed by chemisorbed oxygen species, which is unable to overcome by the low thermal excitation energies, resulting low response. Contrary, at operating temperature beyond 175 °C, the response is <60% and nearly it has decline tendency, which may perhaps be due to the deficiency of active site O^- [34% and 66% of O_2^- & O^- at 225 °C, respectively as shown in Table 1] on the surface of sensor or low interaction of gas molecules with chemisorbed active sites. In other words, we can say that it is because of the low adsorption ability of acetone molecule traces, which caused the low utilization rate on the surface of nanocube In_2O_3@RGO heterostructure. In addition, at higher operating temperatures above 175 °C, more desorption of the adsorbed oxygen ionic species would occur, resulting a low response.

Fig. 4(b) describes the formaldehyde response feature of nanocube In_2O_3@RGO heterostructure based gas sensor as the function of operating temperature. Firstly, low responses (below 15%) were observed by exposing 5–25 ppm HCHO at 125 °C. Subsequently, it is noticed that as working temperature increases, the response to HCHO linearly increases for all concentrations and found to be maximum (~88%) for 25 ppm at 225 °C. It is because of the increase in the density of electrons in the conduction band of sensing material caused by thermal excitation. So, these electrons may be engaged with adsorbed atmospheric oxygen (O_2), reacted and converted it into the active sites (O_2^- and O^-), which is fully responsible for quick and improved gas response [Table 1]. Therefore, adsorbed atmospheric oxygen species on the surface of sensor are considered as one of the most important parameter since illuminating the electronic and chemical peculiarities as well as adsorption ethos of nanocube In_2O_3@RGO heterostructure.[43] Additionally, it is materialize that the RGO acts like a conductor by effectively transferring charge carriers to the sensing electrode at elevated temperature.

On the other hand, the acetone response suddenly decreases and tends to saturate after 175 °C for all concentration [Fig. 4(a)] whereas under the same conditions, the response to HCHO increases throughout [Fig. 4(b)]. The nanocube In_2O_3@RGO heterostructure based gas sensor might have distinct adsorption/desorption and their interaction with acetone traces, therefore it portrays different response to acetone molecule. Further, we can say that the proportions of active site O_2^- slowly decreases and found to be almost mixed states of active sites (O_2^- and O^-) on the sensor surface at all the operating temperatures (beyond 175 °C) for acetone, causes low and saturated response [Fig. 4(a)]. But in the case of formaldehyde, the proportions of O^- active sites increases with increasing the working temperature of sensor and play a crucial role to enhance the sensor response which explores the degree of reactivity with formaldehyde traces. The proportions of active sites (O_2^- and O^-) with operating temperature of sensor for both acetone and formaldehyde are listed in Table 1. However, the adsorption/desorption phenomena occur simultaneously for HCHO because HCHO molecule & its constituents might be easily adsorb and diffuse on the surface of nanocube In_2O_3@-RGO heterostructure based gas sensor. Since, HCHO molecule is an electrophilic, it is Lewis acids having characteristic to

Table 1 The value of proportions [$x(O_2^-)$ and $y(O^-)$] for acetone and formaldehyde based on nanocube In_2O_3@RGO heterostructure gas sensor

| | Participating active sites (O_2^- and O^-) on sensor surface | | | | | | | | | |
| | 125 °C | | 150 °C | | 175 °C | | 200 °C | | 225 °C | |
Test gases	O_2^-	O^-	O_2^-	O^-	O_2^-	O^-	O_2^-	O^-	O_2^-	O^-
$(CH_3)_2CO$	87%	13%	91%	9%	86%	14%	64%	36%	34%	66%
HCHO	99%	1%	78%	22%	51%	49%	46%	54%	4%	96%

Table 2 The response/recovery potential barrier heights for 25 ppm concentration to acetone and formaldehyde at two different operating temperature range

| | Potential barrier heights (meV) | | | |
| | 125–175 °C | | 175–225 °C | |
Test gases	Response (ΔE_{res})	Recovery (ΔE_{rec})	Response (ΔE_{res})	Recovery (ΔE_{rec})
$(CH_3)_2CO$	366	262	189	162
HCHO	333	200	123	93

accept more electrons. Therefore, it is expected to transfer more charges from In_2O_3@RGO heterostructure to the chemisorbed HCHO, resulting an improved response with temperature [Fig. 4(b)].

The gas sensing performances of RGO and In_2O_3 nanocube based gas sensors towards the acetone and formaldehyde have also been studied at the same operating temperature range and concentration as shown in the ESI [Fig. S6(a and b) and S7(a and b)†]. It has been found that the gas sensing response of nanocube In_2O_3@RGO heterostructure based acetone and formaldehyde sensor is higher compared to the bare RGO and In_2O_3 nanocube based gas sensor. This enhanced sensing execution of nanocube In_2O_3@RGO heterostructure based gas sensor is attributed to the synergistic effect between the RGO and In_2O_3 nanocube.

Consequently, the optimum working temperature for nanocube In_2O_3@RGO heterostructure based gas sensor to discriminate 25 ppm concentration of acetone and formaldehyde is 175 °C and 225 °C, respectively, which are immaculate from the viewpoint of chemiresistive gas sensors. Therefore, the optimum working temperature 175 °C for acetone and 225 °C for formaldehyde have been preferred to further study other characteristics *e.g.* response/recovery times, selectivity and lifetime of nanocube In_2O_3@RGO heterostructure based gas sensor.

Acetone and formaldehyde gas sensing mechanisms and calculation of active sites (O_2^- & O^-). When the ppm level concentrations of acetone and formaldehyde are injected into the test gas chamber, the electrical resistance of nanocube In_2O_3@RGO heterostructure based gas sensor decreases and it again increases when their supply is stopped and air is naturally poured. These gas sensing characteristics can be explained by the change of electrical resistance which may be due to the

adsorbed active sites on the surface of sensor and reaction with the test gas molecules.[44] Atmospheric oxygen is adsorbed on the surface of nanocube In_2O_3@RGO heterostructure based gas sensor in different forms varying from molecular form (physisorption) to dissociative form (chemisorption) depending on the working temperature. The oxygen species O_2^-, O^- and O^{2-} formed on the surface of nanocube In_2O_3@RGO heterostructure based gas sensor at different operating temperatures, induce an electron depletion layer, resulting a decrease/increase in carrier concentration and an increase/decrease in surface potential barrier heights. After exposing the acetone and formaldehyde in the test chamber, the surface oxygen is participated due to the chemical reaction.[45]

$$O_2(gas) \leftrightarrow O_2(phys) \leftrightarrow O_2^-(chem) \leftrightarrow 2O^-(chem) \leftrightarrow 2O^{2-}(chem) \quad (2)$$
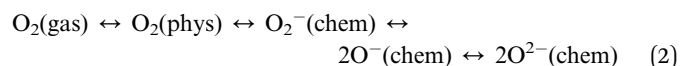
Therefore, concentration of the surface oxygen species depends not only on the concentration of the reducing gases but also the working temperature of sensor. The chemical adsorption of oxygen and its reactions with acetone and formaldehyde follow the sensing mechanisms of nanocube In_2O_3@RGO heterostructure based gas sensor. Therefore, eqn (1) can be written below in terms of concentration,[45]

$$S = \frac{R_{air} - R_{(CH_3)_2CO/HCHO}}{R_{air}} \times 100\% \propto C_{(CH_3)_2CO/HCHO}{}^n \quad (3)$$

where $C_{(CH_3)_2CO/HCHO}$ is the concentration of acetone and formaldehyde and the power law exponent "n". The theoretical value of exponent "n" in above equation is 1, 0.5 and 0.25 depending on the chemisorbed oxygen species O_2^-, O^- and O^{2-}, respectively and also on the operating temperature.[45]

The acetone and formaldehyde sensing mechanisms and the proportions of involved active sites (O_2^- and O^-) were calculated by the following reactions.

$$CH_3COCH_3 + xO_2^- + 6yO^- \rightarrow 3CO_2 + 3H_2O + (x + 6y)e^- \quad (4)$$
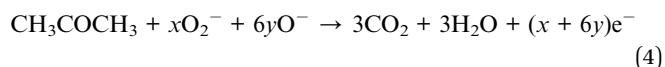
$$x + y = 1 \quad (4a)$$

here, x and y are the proportions of active sites O_2^- and O^-, respectively. Therefore, value of exponent "n" was calculated in terms of proportions "y" by using eqn (4) & (4a),

$$n = 1/(1 + 5y) \quad (4b)$$

Inserting, the value of "n" from eqn (4b) to eqn (3), we obtain,

$$S \propto C_{(CH_3)_2CO}^{1/1+5y} \qquad (4c)$$

Similarly for formaldehyde,

$$HCHO + xO_2^- + 2yO^- \rightarrow CO_2 + H_2O + (x + 2y)e^- \qquad (5)$$

$$x + y = 1 \qquad (5a)$$

$$n = 1/(1 + y) \qquad (5b)$$

$$S \propto C_{HCHO}^{1/1+y} \qquad (5c)$$

Further, the eqn (4c) & eqn (5c) were plotted and demonstrated in Fig. 5(a and b) with the help of gas response data [Fig. 4(a and b)], to calculate the power law exponent "n" [slopes of Fig. 5(a and b)] and the value of x & y, the proportions of active
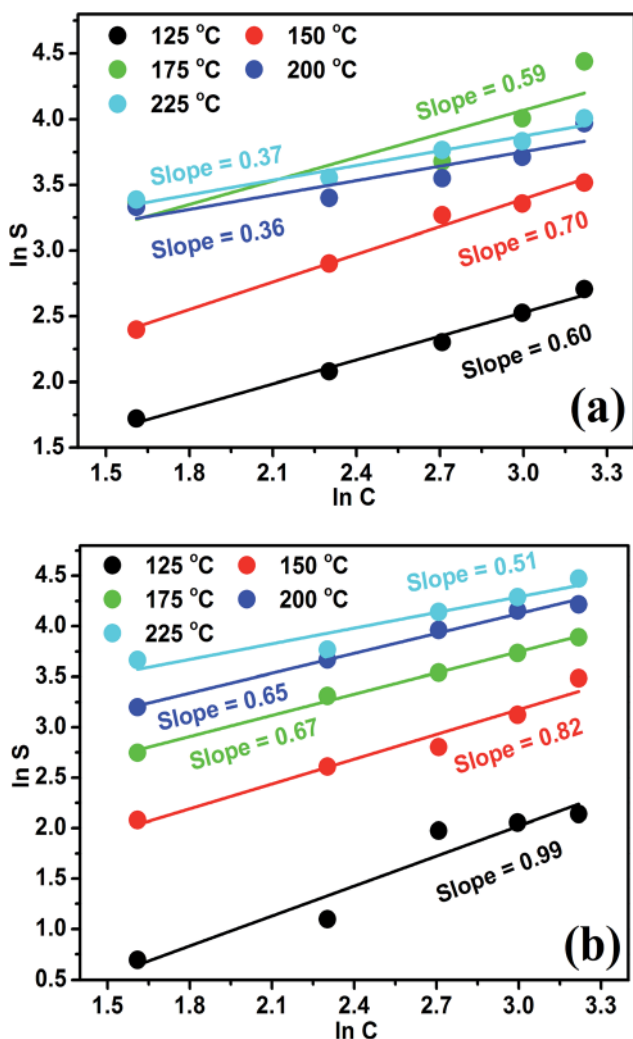

Fig. 5 Logarithm plots of acetone (a) and HCHO (b) responses (S) as a function of (5, 10, 15, 20 and 25 ppm) concentration (C) at various operating temperatures (the dots are experimental data and lines are the linear fitting function).

sites (O_2^- and O^-), which are participating actively in the sensing mechanism of acetone and formaldehyde. Fig. 5(a and b) shows the logarithm plots of acetone and formaldehyde as the function of gas concentrations at various operating temperatures. It has been observed that the values of exponent "n", listed in the Table 1, were different at distinct operating temperatures, indicating towards the existence of different proportions of ionosorbed oxygen species $e.g.$ O_2^- or O^- or both (O_2^- & O^-) on the surface of nanocube In_2O_3@RGO heterostructure based gas sensor. For example, $n = 0.59$ at 175 °C for acetone as shown in Fig. 5(a), it means, the experimental result lies between the theoretical values $0.5 < n < 1$. By incorporating the value of "n" into the eqn (4c) and also using eqn (4a) & (4b) leads to: $x = 0.87$, $y = 0.13$. Thus, oxygen might be adsorbed on the surface of nanocube In_2O_3@RGO heterostructure based gas sensor in the form of O_2^- (87%) and O^- (13%), respectively. On the other hand, $n = 0.51$ at 225 °C for formaldehyde as calculated from Fig. 5(b), lies between the theoretical values $0.5 < n < 1$. Fascinatingly, this value put into eqn (5c) and also using eqn (5a) & (5b) to evaluate $x = 0.04$ and $y = 0.96$. So, the active sites O_2^- (4%) and O^- (96%) may be adsorbed on the surface of sensor and play a crucial role in the gas sensing performance. Finally, we concluded that the power law eqn (4c) and (5c) are the characteristics of surface reactions and provide insight view about the dominating species of oxygen adsorbates.

Response/recovery dynamic analyses of nanocube In_2O_3@ RGO heterostructure based acetone and formaldehyde sensor. The response/recovery real-time analyses have been investigated for the basic understanding of gas sensing mechanisms along with its correlation with the surface adsorbed oxygen species. The response time (τ_{res}) is basically defined as the time taken by the sensor to read maximum fluctuations in the resistance (normally 90%) upon exposure to test gases (acetone and formaldehyde) while recovery time (τ_{rec}) is defined as the time taken by the sensor to return to its original situation under the absence of test gases. Fig. 6(a and b) illustrate the real-time response characteristics of acetone and formaldehyde for 5–25 ppm concentrations at different working temperatures of 175 °C and 225 °C, respectively.

Fig. 6(a and b) show that the response time are decreasing with increasing gas concentration as well as temperature (175 & 225 °C) but the recovery time somehow is influenced and increased. It might be due to the dense surrounding around the surface of sensor, and subsequently slow adsorption/desorption reaction rate on the sensor surface which results in enhanced recovery time. It has been instituted from Fig. 6(a and b) that the response/recovery times of formaldehyde are less compared to acetone, demonstrating electrophilic nature of formaldehyde.

According to the solid state physics of matter, the well-known relation of thermal activation function which represents the relation between the response/recovery time constants as a function of temperature is written below:[46]

$$\tau_{res} = \tau_{res}^0 \exp(\Delta E_{res}/K_B T) \qquad (6)$$

$$\tau_{rec} = \tau_{rec}^0 \exp(\Delta E_{rec}/K_B T) \qquad (7)$$
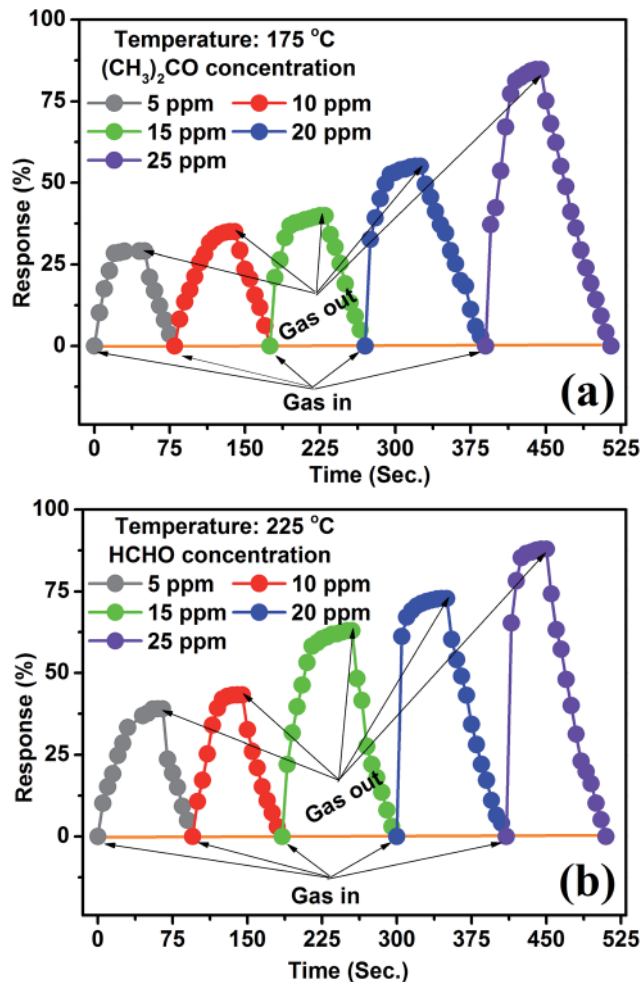
Fig. 6 The response/recovery real time profiles of the nanocube In$_2$O$_3$@RGO heterostructure based gas sensor to acetone (a) and formaldehyde (b) for 5–25 ppm concentration at optimum working temperature 175 °C and 225 °C, respectively.
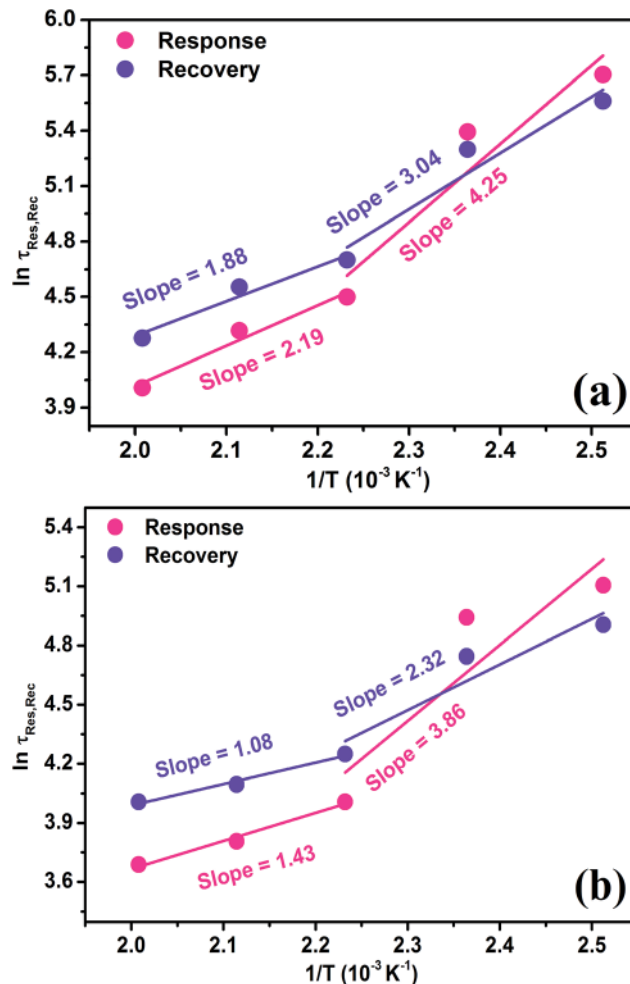

Fig. 7 Logarithm plots of response/recovery reaction time to 25 ppm of acetone (a) and HCHO (b) as a function of reverse of temperature (dots are experimental data and lines are the linear fitting functions).

where, τ_{res}^0, τ_{rec}^0, K_B and T are time coefficients, Boltzmann's constant and absolute temperature, respectively. The τ_{res}, τ_{rec}, ΔE_{res} and ΔE_{rec} represent the response, recovery reaction times response and recovery reaction potential barrier heights, respectively.

Eventually, we employed eqn (6) and (7) for the calculation of response/recovery potential barrier heights with the help of response and recovery reaction time for 25 ppm concentration to acetone and formaldehyde at different operating temperatures by using the experimental data as presented in Fig. S8(a and b).† Fig. 7(a and b) show the logarithm plots of response/recovery reaction time as a function of reverse of temperature for 25 ppm concentration to acetone and formaldehyde. It is observed that the response/recovery reaction time increases with decreasing the operating temperatures for both the test gases. It is also found that at low operating temperatures, the response reaction time are little bit longer compared to the recovery reaction time for both the test gases.

Interestingly, it has been also noticed that at higher operating temperatures, the response reaction time are low with

respect to recovery reaction time for both the gases. It may perhaps be depend on adsorbed active sites on the sensor surface and potential barrier height, which is summarized in Tables 1 and 2, respectively. By linear fitting [Fig. 7(a and b)], we calculated the response/recovery reaction potential barrier heights in between the two temperature ranges (125–175 °C & 175–225 °C) and is summarized in Table 2. It is observed that the response/recovery potential barrier heights (ΔE_{res} and ΔE_{rec}) are fairly distinct, unveiling two different mechanisms at 125–175 °C and 175–225 °C. These, ΔE_{res} and ΔE_{rec} values are in good agreement with solid state theoretical relations [eqn (6) and (7)], indicating that it is proportional to the τ_{res} and τ_{rec} time and inversely proportional to operating temperature of the sensor [Table 2].

The response/recovery reaction time are dominated by the heights of potential barrier. Determined as, the ΔE_{res} and ΔE_{rec} for acetone are little bit more compared to the formaldehyde for all working temperatures and also found to be reduced at higher temperature [Table 2]. It is attributed to thermal excitation of electrons thereby swing in Fermi level between the

valance band and conduction band of nanocube In_2O_3@RGO heterostructure, pointing towards quick response/recovery times of In_2O_3@RGO heterostructure based acetone and formaldehyde sensor Fig. 6(a and b). These facts indicate that the both response and recovery reactions are easy to take place. It may take place due to the other factors such as grain boundaries, size of grains, sensor surface reaction rates and diffusion reaction rates which are affecting the response/recovery reaction rates. There are several other unknown factors which may also play a crucial role in the sensing response/recovery time and needed to be addressed. These results also validate all finding as addressed above in Fig. 4(a and b), 5(a and b) and 6(a and b).

Selectivity study of nanocube In_2O_3@RGO heterostructure based acetone and formaldehyde sensor. To further explore the applicability, the nanocube In_2O_3@RGO heterostructure based gas sensor has been implemented for the selective detection of acetone and formaldehyde in the presence of multifarious meddling gases in the environment. In this study, the meddling gases such as ethanol (C_2H_5OH), methanol (CH_3OH), chloroform ($CHCl_3$), toluene (C_7H_8), benzene (C_6H_6), ammonia (NH_3), formic acid (CH_2O_2) and acetic acid ($C_2H_4O_2$) have been used to calibrate the selective nature of the nanocube In_2O_3@RGO heterostructure based acetone and formaldehyde sensor.

Fig. 8(a and b) depict the selective responses of nanocube In_2O_3@RGO heterostructure sensor in the presence of other meddling gases for fixed concentration (25 ppm) to acetone and formaldehyde at two working temperatures of 175 °C and 225 °C, respectively. Fig. 8(a) illustrates the selectively higher response (~85%) to acetone whereas Fig. 8(b) displays the high selective performance (~88%) to formaldehyde for the same concentration at two different operating temperature of 175 °C and 225 °C, respectively compared to the other meddling gases present in the environment, and nearly no other responses of meddling gases were observed.

In other words, as demonstrated in Fig. 8(a and b), both kinds of sensors based on nanocube In_2O_3@RGO heterostructure possess good selectivity to recognize acetone at 175 °C and formaldehyde at 225 °C, which is almost insensitive to other typical meddling gases at the same concentration and temperature. It may be due to the presence of sufficient active sites (O_2^- and O^-) on the surface of sensor and their good interaction with the test gases. Thus, our experimental observations suggest that the nanocube In_2O_3@RGO heterostructure based gas sensor works not only to recognize the test gases but also provide good discrimination of an individual gas from the bundle of gases, used for the experimentation.

In order to quantitatively calibrate the selectivity of acetone and formaldehyde from the environment, we have employed the following relation to determine the selectivity coefficient (K_{sc}) in the presence of different meddling gases.[28]

$$K_{sc} = \frac{S_{acetone/formaldehyde}}{S_{gas}} \qquad (8)$$

where, $S_{acetone/formaldehyde}$ and S_{gas} are the responses of the sensor in acetone & formaldehyde and additional interfering gases.

The selectivity coefficients are summarized in the Table 3. The selectivity coefficient for nanocube In_2O_3@RGO heterostructure material based acetone sensor functioned at 175 °C for 25 ppm is highest to $C_2H_4O_2$ (18.8) while for RGO/In_2O_3 nanocube hybrid material based formaldehyde sensor worked at 225 °C for 25 ppm is found to be maximum for $C_2H_4O_2$ (10.9). Therefore, it suggests that the nanocube In_2O_3@RGO heterostructure sensor shows good selective detection to acetone and formaldehyde compared to $C_2H_4O_2$ *e.g.* the gas response to acetone and formaldehyde are 18.8 and 10.9 times, respectively higher than to $C_2H_4O_2$.

Life-time study of nanocube In_2O_3@RGO heterostructure based acetone and formaldehyde sensor. The long-term endurance is one of the most important characteristics of the sensor devices from the perspective of practical applications. The long-term stable nature at which the nanocube In_2O_3@RGO heterostructure based gas sensor detects utmost response of 25 ppm concentration to acetone and formaldehyde at optimum working temperatures of 175 °C and 225 °C, respectively, has been examined for 30 days over an interval of 5 days as depicted in Fig. 9. It is noticed that the responses were slightly reduced by ~7% to acetone and ~3% to formaldehyde during sensor experimentation. It is due to good mutual interaction between the acetone/formaldehyde and surface of sensor
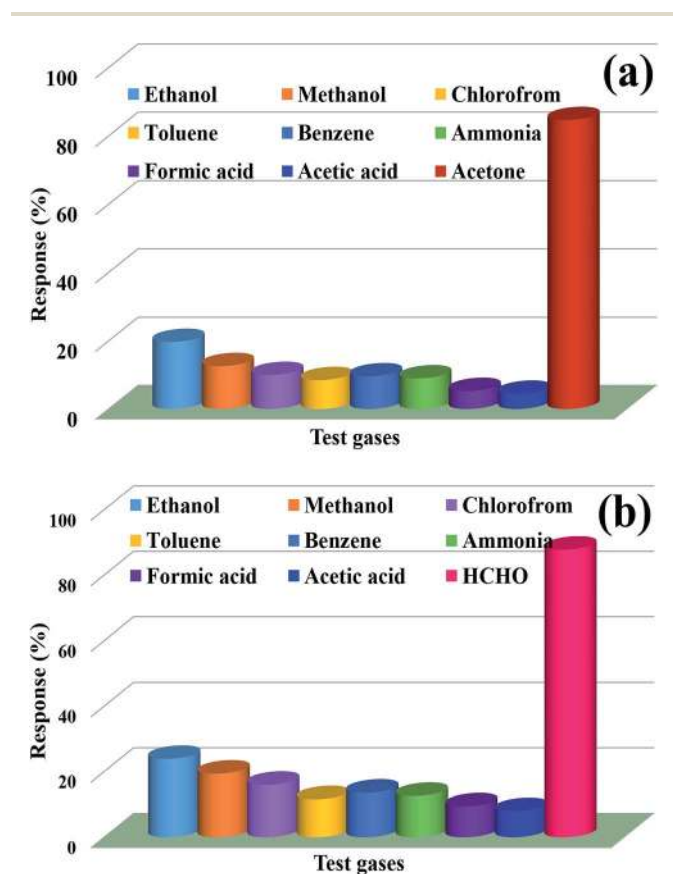
Fig. 8 Selectivity profiles for 25 ppm concentration of acetone (a) and formaldehyde (b) at optimum working temperature 175 °C and 225 °C, respectively, based on nanocube In_2O_3@RGO heterostructure gas sensor.

Table 3 The selectivity coefficient "K_{sc}" of the nanocube In_2O_3@RGO heterostructure based acetone and formaldehyde sensor to different meddling gases for 25 ppm concentration at optimum working temperature 175 °C and 225 °C, respectively

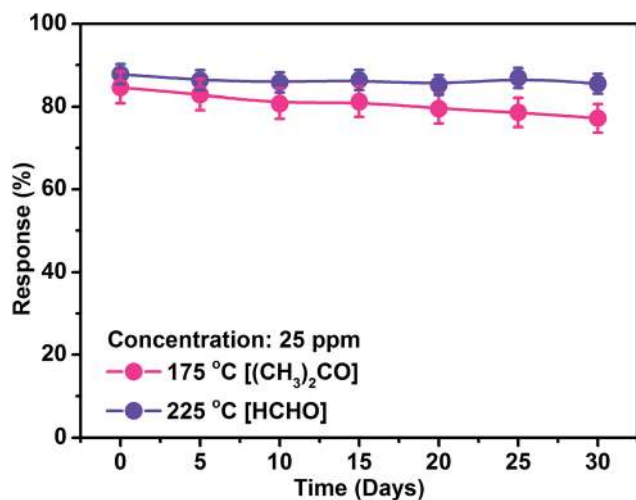| Sensing devices	Meddling gases with 25 ppm concentration							
	C_2H_5OH	CH_3OH	$CHCl_3$	C_7H_8	C_6H_6	NH_3	CH_2O_2	$C_2H_4O_2$
Nanocube In_2O_3@RGO heterostructure based $(CH_3)_2CO$ sensor (175 °C)	4.3	6.7	8.5	9.9	8.8	9.4	15.9	18.8
Nanocube In_2O_3@RGO heterostructure based HCHO sensor (225 °C)	3.7	4.5	5.5	7.6	6.5	6.9	9.3	10.9

Fig. 9 Life-time performances of nanocube In_2O_3@RGO heterostructure based gas sensor functioned at 175 °C and 225 °C for 25 ppm concentration to acetone and formaldehyde, respectively.

compared to the other interfering gases or low potential barrier heights, which are responsible for the fast reactions and the rate of adsorption–desorption increases due to the increased diffusivity of the gases, results longer life. Therefore, the lasting performance of the sensor to 25 ppm acetone and formaldehyde at 175 °C & 225 °C, respectively, demonstrated the stable nature and magnificent robustness of the nanocube In_2O_3@RGO heterostructure.

Conclusions

In conclusion, the nanocube In_2O_3@RGO heterostructure as well as bare In_2O_3 nanocubes were synesized *via* surfactant assisted hydrothermal method. The nanocube In_2O_3@RGO heterostructure based gas sensor showed better response for 25 ppm concentration to acetone and formaldehyde at 175 °C and 225 °C compared to the bare RGO and In_2O_3 nanocube based gas sensor. Our experimental findings would make a meaningful contribution towards the fabrication of nanocube In_2O_3@RGO heterostructure based gas sensor to recognize acetone and formaldehyde with excellent gas sensing performance such as high response, excellent selectivity with good long-term stability and quick response/recovery. It could be concluded that the nanocube In_2O_3@RGO heterostructure based gas sensor is promising for air quality monitoring of VOCs.

Notes and references

1 E.-X. Chen, H. Yang and J. Zhang, *Inorg. Chem.*, 2014, **53**, 5411–5413.
2 P. Offermans, M. Crego-Calama and S. H. Brongersma, *Nano Lett.*, 2010, **10**, 2412–2415.
3 N. Yamazoe, *Sens. Actuators, B*, 2005, **108**, 2–14.
4 Y. Shimizu and M. Egashira, *MRS Bull.*, 1999, **24**, 18–24.
5 S. B. Upadhyay, R. K. Mishra and P. P. Sahay, *Sens. Actuators, B*, 2015, **209**, 368–376.
6 Y. Xiao, L. Lu, Ai. Zhang, Y. Zhang, L. Sun, L. Huo and F. Li, *ACS Appl. Mater. Interfaces*, 2012, **4**, 3797–3804.
7 S. Elouali, L. G. Bloor, R. Binions, I. P. Parkin, C. J. Carmalt and J. A. Darr, *Langmuir*, 2012, **28**, 1879–1885.
8 Y. Shigesato, S. Takaki and T. Haranoh, *J. Appl. Phys.*, 1992, **71**, 3356–3364.
9 Q. Liu, W. Lu, A. Ma, J. Tang, J. Lin and J. Fang, *J. Am. Chem. Soc.*, 2005, **127**, 5276–5277.
10 G. Shen, B. Liang, X. Wang, H. Huang, D. Chen and Z. L. Wang, *ACS Nano*, 2011, **5**, 6148–6155.
11 C.-Y. Huang, G.-C. Lin, Y.-J. Wu, T.-Y. Lin, Y.-J. Yang and Y.-F. Chen, *J. Phys. Chem. C*, 2011, **115**, 13083–13087.
12 P.-C. Chen, G. Shen, S. Sukcharoenchoke and C. Zhou, *Appl. Phys. Lett.*, 2009, **94**, 043113.
13 X. Zou, X. Liu, C. Wang, Y. Jiang, Y. Wang, X. Xiao, J. C. Ho, J. Li, C. Jiang, Q. Xiong and L. Liao, *ACS Nano*, 2013, **7**, 804–810.
14 G. Shen, J. Xu, X. Wang, H. Huang and D. Chen, *Adv. Mater.*, 2011, **23**, 771–775.
15 K. R. R. Gil, Y. Sun, E. R. García and D. Raftery, *J. Phys. Chem. C*, 2009, **113**, 12558–12570.
16 H. Jia, Y. Zhang, X. Chen, J. Shu, X. Luo, Z. Zhang and D. Yu, *Appl. Phys. Lett.*, 2003, **82**, 4146–4148.
17 L.-C. Chen, C.-H. Tien and W.-C. Liao, *J. Phys. D: Appl. Phys.*, 2011, **44**, 165101.
18 N. G. Pramod and S. N. Pandey, *Ceram. Int.*, 2014, **40**, 3461–3468.

19 J. Kim, Y. S. Rim, H. Chen, H. H. Cao, N. Nakatsuka, H. L. Hinton, C. Zhao, A. M. Andrews, Y. Yang and P. S. Weiss, *ACS Nano*, 2015, **9**, 4572–4582.

20 M. Curreli, C. Li, Y. Sun, B. Lei, M. A. Gundersen, M. E. Thompson and C. Zhou, *J. Am. Chem. Soc.*, 2005, **127**, 6922–6923.

21 X. S. Niu, H. X. Zhong, X. J. Wang and K. Jiang, *Sens. Actuators, B*, 2006, **115**, 434–438.

22 J. Q. Xu, Y. P. Chen, Q. Y. Pan, Q. Xiang, Z. X. Cheng and X. W. Dong, *J. Nanotechnol.*, 2007, **18**, 115615.

23 (*a*) A. K. Geim and K. S. Novoselov, *Nat. Mater.*, 2007, **6**, 183–191; (*b*) M. Srivastava, J. Singh, T. Kuila, R. K. Layek, N. H. Kim and J. H. Lee, *Nanoscale*, 2015, **7**, 4820–4868; (*c*) M. Kim, R. K. Mishra, R. Manda, G. Murali, T.-H. Kim, M.-H. Lee, M. Yun, S. Kundu, B.-S. Kim and S. H. Lee, *RSC Adv.*, 2017, **7**, 16650–16654.

24 (*a*) A. K. Geim, Graphene: status and prospects, *Science*, 2009, **324**, 1530–1534; (*b*) M. Srivastava, Md. E. Uddin, J. Singh, N. H. Kim and J. H. Lee, *J. Alloys Compd.*, 2014, **590**, 266–276; (*c*) M. Srivastava, A. K. Das, P. Khanra, Md. E. Uddin, N. H. Kim and J. H. Lee, *J. Mater. Chem. A*, 2013, **1**, 9792–9801.

25 S. Y. Jeong, S. Jeong, S. W. Lee, S. T. Kim, D. Kim, H. J. Jeong, J. T. Han, K.-J. Baeg, S. Yang, M. S. Jeong and G.-W. Lee, *Sci. Rep.*, 2015, **5**, 11216.

26 J.-H. Chang, W.-H. Lin, P.-C. Wang, J.-I. Taur, T.-A. Ku, W.-T. Chen, S.-J. Yan and C.-I. Wu, *Sci. Rep.*, 2015, **5**, 9693.

27 J.-H. Son, S.-J. Baeck, M.-H. Park, J.-B. Lee, C.-W. Yang, J.-K. Song, W.-C. Zin and J.-H. Ahn, *Nat. Commun.*, 2014, **5**, 3484.

28 H. Park, S. Chang, M. Smith, S. Gradečak and J. Kong, *Sci. Rep.*, 2013, **3**, 1581.

29 R. Raccichini, A. Varzi, S. Passerini and B. Scrosati, *Nat. Mater.*, 2015, **14**, 271–279.

30 J.-H. Ahn and B. H. Hong, *Nat. Nanotechnol.*, 2014, **9**, 737–738.

31 S. Some, Y. Xu, Y. Kim, Y. Yoon, H. Qin, A. Kulkarni, T. Kim and H. Lee, *Sci. Rep.*, 2013, **3**, 1868.

32 X. Sun, H. Hao, H. Ji, X. Li, S. Cai and C. Zheng, *ACS Appl. Mater. Interfaces*, 2014, **6**, 401–409.

33 S. Ju, K.-Y. Lee, S.-J. Min, Y. K. Yoo, K. S. Hwang, S. K. Kim and H. Yi, *Sci. Rep.*, 2015, **5**, 9196.

34 H. G. Moon, Y.-S. Shim, D. H. Kim, H. Y. Jeong, M. Jeong, J. Y. Jung, S. M. Han, J. K. Kim, J.-S. Kim, H.-H. Park, J.-H. Lee, H. L. Tuller, S.-J. Yoon and H. W. Jang, *Sci. Rep.*, 2012, **2**, 588.

35 X. Lai, D. Wang, N. Han, J. Du, J. Li, C. Xing, Y. Chen and X. Li, *Chem. Mater.*, 2010, **22**, 3033–3042.

36 W. Yang, P. Wan, X. Zhou, J. Hu, Y. Guan and L. Feng, *ACS Appl. Mater. Interfaces*, 2014, **6**, 21093–21100.

37 Q. Huang, D. Zeng, H. Li and C. Xie, *Nanoscale*, 2012, **4**, 5651–5658.

38 R. K. Mishra, S. B. Upadhyay, A. Kushwaha, T.-H. Kim, G. Murali, R. Verma, M. Srivastava, J. Singh, P. P. Sahay and S. H. lee, *Nanoscale*, 2015, **7**, 11971–11979.

39 J. M. Du, L. Huang and Z. Q. Chen, *J. Phys. Chem. C*, 2009, **113**, 9998.

40 A. Gurlo, N. Barsan, U. Weimar, M. Ivanovskaya, A. Taurino and P. Siciliano, *Chem. Mater.*, 2003, **15**, 4377.

41 J. Cao, H. Dou, H. Zhang, H. Mei, S. Liu, T. Fei, R. Wang, L. Wang and T. Zhang, *Sens. Actuators, B*, 2014, **198**, 180–187.

42 H. Mu, K. Wang, Z. Zhang and H. Xie, *J. Phys. Chem. C*, 2015, **119**, 10102–10108.

43 R. A. Kadir, Z. Li, A. Z. Sadek, R. A. Rani, A. S. Zoolfkar, M. R. Field, J. Z. Ou, A. F. Chrimes and K. Kalantar-zadeh, *J. Phys. Chem. C*, 2014, **118**, 3129–3139.

44 S. Bai, S. Chen, Y. Zhao, T. Guo, R. Luo, D. Li and A. Chen, *J. Mater. Chem. A*, 2014, **2**, 16697–16706.

45 L. Mei, Y. Chen and J. Ma, *Sci. Rep.*, 2014, **4**, 6028.

46 R. Xing, L. Xu, J. Song, C. Zhou, Q. Li, D. Liu and H. W. Song, *Sci. Rep.*, 2015, **5**, 10717.